Post-Print of an Accepted Manuscript on the Laboratory of Turbulent Flows Website

Complete citation:

Wang, S., & Ghaemi, S. (2021). Full-Span Topology of Trailing-Edge Separation at Different Angles of Attack. *AIAA Journal*, *59*(12), 5186-5197. doi: 10.2514/1.J060337

The final publication is available at https://doi.org/10.2514/1.J060337

The Accepted Manuscript begins on the next page.

Full-span Topology of Trailing-edge Separation at Different Angles of Attack

Sen Wang[1] and Sina Ghaemi[2]

The University of Alberta, Edmonton, Alberta, T6G 1H9, Canada

The velocity field over a two-dimensional wing at Reynolds number of 672,000 was investigated to characterize the 3D topology and evolution of the separate flow with variation of the angle-of-attack. Planar particle image velocimetry over the full-span of the wing demonstrated that with increasing angle-of-attack, isolated pockets of backflow, that appeared near the trailing edge, merged and formed an asymmetric stall cell at angle-of-attack of 9.7°. The asymmetry was mainly associated with the dissimilar boundary layers developed on the wind tunnel walls at the spanwise ends of the wing. Secondary structures were also observed between the stall cell and the spanwise end. The stall cell topology was characterized using large-scale three-dimensional particle tracking velocimetry measurements utilizing helium-filled soap bubbles. The results showed that the separation bubble had a small wall-normal height with two wall-normal counter-rotating vortices extended up to the edge of the separation bubble. In addition, the investigations demonstrated that vortex generators can induce a symmetric stall cell by removing the secondary structures and isolating the stall cell from the flows at the spanwise ends.

Nomenclature

c = chord, mm

h = vortex generator height, mm

l = spanwise distance between the saddle point and the focus point, mm

Re_c = chord-based Reynolds number, $\rho U_\infty c/\mu$

s = span, mm

[1] PhD Student, Department of Mechanical Engineering, The University of Alberta.
[2] Associate Professor, Department of Mechanical Engineering, The University of Alberta, ghaemi@ualberta.ca (Corresponding Author).

U = streamwise velocity, m/s

U_∞ = freestream velocity, m/s

x = streamwise direction

y = wall-normal direction

z = spanwise direction

α = angle of attack, degree

β = incidence angle of vortex generators vanes, degree

μ = dynamic air viscosity, kg/ms

ρ = air density, kg/m^3

I. Introduction

Flow Separation at high angles-of-attack (α) limits the aerodynamic performance of aircraft wings and high-lift devices by increasing drag and reducing lift. During flow separation, the boundary layer (BL) flow loses its streamwise momentum and moves away from the wing surface [1-3]. In investigations that assumed the separated flow was uniform in spanwise direction, i.e., two dimensional (2D), the separation point was simply indicated as the location of zero wall-shear-stress [3, 4]. However, flow separation typically does not form a 2D flow pattern. In most applications, including flow over 2D wings, the separated flow forms a three-dimensional (3D) pattern in which separation occurs along an axis, where the streamlines converge and lift-up from the surface. This axis is known as a separation/detachment line and crosses through a saddle-type critical point [5, 6].

The skin-friction patterns obtained from different visualization techniques have often been used to identify different topologies associated with separated flows. An early investigation by Moss and Murdin [7] observed a large mid-span separation zone with two wall-normal counter-rotating vortices on a NACA 0012 airfoil using oil flow visualization. The oil-flow visualization made by Dell'Orso and Amitay [8] also showed that the flow over a 2D wing can form different patterns including an asymmetric full-span separation, 3D separation with mid-span recirculation, or 3D separation with one or multiple stall cells (SCs). Among these patterns, the SC has drawn particular attention due to its unique cellular organization. Flow visualizations, using oil [9] and tufts [10], have shown that the SC has a spanwise separation line that spirals from both ends into two counter-rotating foci, forming a mushroom-shape pattern. It is also known that SCs only form for certain airfoils and under specific flow conditions. For example, Dell'Orso and Amitay [8] observed SCs for moderate to high chord-based Reynolds number of $Re_c = 10^5$ to 10^6 [8]. Broeren and

Bragg [11] experimentally showed that thin airfoils that undergo leading-edge flow separation do not exhibit a SC pattern. They observed SCs only for thicker airfoils with trailing-edge (TE) separation. The SC pattern has been reported for both pre-stall [12-14] and post-stall [7, 9, 10, 15-17] conditions, defined relative to the α that corresponds to maximum steady lift.

In an early investigation, Weihs and Katz [9] hypothesized that the foci of SCs extend into a pair of counter-rotating streamwise vortices that are connected to each other, and form a loop in the wake region. Later, Yon and Katz [10] proposed a different topology model in which the counter-rotating vortices only extend in the streamwise direction without forming a closed loop. Manolesos and Voutsinas [12] performed numerical flow simulations and stereoscopic particle image velocimetry (stereo-PIV) measurements of the separated flow over a 2D wing with an aspect ratio (AR) of 2 at α = 10° and Re_c of 8.7×10^5. Their results showed that the SC exhibited a pair of counter-rotating vortices, which were normal to the wing surface and gradually aligned with the freestream flow as they traveled downstream. They also identified two spanwise vortices: a separation line vortex slightly upstream of the TE, and a trailing-edge vortex immediately downstream of the TE. To further investigate the flow structure associated with SC under different flow conditions, Dell'Orso et al. [17] performed stereo-PIV measurements on a NACA 0015 airfoil with AR = 4 at α = 16° and Re_c of 3.55×10^5. A zig-zag tape was installed close to the leading edge to form a SC at the midspan of the wing. Their measurements captured the spanwise vortex but did not show any clear evidence of streamwise vortices within the SC. A latter stereo-PIV measurement by Dell'Orso and Amitay [8] on the same airfoil at α = 16.5° and Re_c of 4.11×10^5 captured a pair of streamwise vortices upstream of the TE. Since the flow condition of the two investigations is similar, the disagreement is potentially due to the use of the zig-zag tape in Dell'Orso et al. [17]. For a pre-stall condition, a recent experimental study by Ma et al. [13] at Re_c of 7.5×10^5 showed that a large SC pattern only exists in the mean flow field while the instantaneous flow includes SC patterns that are an order of magnitude smaller. The contradictory observations regarding the topology of the vortices associated with SCs indicate that their 3D topology is yet to be characterized at various flow conditions.

Several investigations were conducted to explore the SC patterns at different experimental conditions including AR, α, and Re_c. For a Clark Y airfoil at a post-stall α of 18.4° at Re_c of 3.85×10^5, Winkelmann and Barlow [16] demonstrated that the number of SCs over the span of the wing increased when AR increased from 3 to 12. Based on oil-flow visualization and crow-type instability [18], Weihs and Katz [9] formulated a linear relation between the number of SCs and AR. Yon and Katz [10] performed a study on the SC structures occurring on a post-stall airfoil at

α = 17° and Re_c of 6.2 × 10^5. Using tuft visualization, they observed that the number of SCs was proportional to AR. The number of SCs observed by the recent investigation of Dell'Orso and Amitay [8] agreed with the relation proposed by Weihs and Katz [9]. Previous investigations have shown that the number of SCs also depends on the α. Boiko et al. [14] observed five SCs at α = 9.1°, while increasing α resulted in SCs to expand and merge. At α = 18.4°, they observed a single large SC covering the full span of the wing. Dell'Orso and Amitay [8] observed that with increasing α from 15° to 21.5°, the flow pattern developed from an asymmetric full-span separation into a single SC and eventually into a dual SC pattern. The results from Boiko et al. [14] and Dell'Orso and Amitay [8] appear to contradict each other, possibly due to the differences in the airfoil shape. Regarding the effect of Re_c, Dell'Orso and Amitay [8] showed that at a fixed α of 17, the flow pattern changed from an asymmetric full-span separation to an asymmetric SC with increasing Re_c from 3.02 × 10^5 to 4.47 × 10^5. They also observed a critical Re_c, below which a SC did not form [8]. This critical Re_c was observed to increase with increasing α. However, this appears to be in contrast to the results of Manolesos and Voutsinas [19] in which the critical Re_c reduced with increasing α. The experiment of Manolesos and Voutsinas [19] was at a higher range of Re_c from 5 × 10^5 to 1.5 × 10^6 and pre-stall α of 6° to 9°.

The formation mechanism of SCs was also studied in the past decades. Weihs and Katz [9] hypothesized that SCs form due to the cross-span wavy disturbances produced by the interaction between the leading-edge and trailing-edge vortex lines, and the wing surface [18]. The theory was supported by the experiments of Broeren and Bragg [11], which demonstrated that the SC exists on thick airfoils with trailing-edge separation for which the leading-edge and trailing-edge vortices are closer. The oil-flow visualization of Dell'Orso and Amitay [8] also supported the theory by showing that the formation of SC was associated with the interaction between these two vortex lines. Moss and Murdin [7] showed that by adding a disturbance using roughness elements near the leading edge, the SC can form at a lower α than the undisturbed flow. Similar observations connecting the formation of SC with the spanwise disturbances were also made in later studies [17, 20-24]. Rodíguez and Theofilis [25, 26] observed that the SC pattern can be obtained by linear superimposition of a steady laminar 2D flow with the dominant global eigenmode of its separated flow.

Previous investigations using tuft [10], and oil-flow visualizations [8, 9, 15, 16, 27, 28] showed that the pattern of multiple SCs is usually asymmetric in the spanwise direction; the SCs can be different in size and they do not organize symmetrically. Even in separated flows with only one SC, the pattern can be asymmetric, and the centerline of the SC may deviate from the midspan of the airfoil [8, 11, 12, 29]. These asymmetries are speculated to be due to several factors such as asymmetry in the corner flows near the spanwise ends of the airfoil, imperfections of the airfoil, and

non-uniformity of the freestream flow. The asymmetry in SC patterns of the previous investigations poses a challenge in the repeatability and the comparison of experimental results. To study the formation mechanism and to compare experimental results, it is of interest to identify the source of asymmetry and to generate symmetric SCs. For example, Yon and Katz [10] installed tip plates at the spanwise ends of a wing to reduce the effect of tip vortices and wall-interference. They compared their results with Winkelmann and Barlow [16] and concluded that the tip plates result in a greater number of SCs over the wingspan. In another experiment, Gregory et al. [30] employed suction perforations on the spanwise ends of the airfoil and the wind tunnel walls. Such techniques for imposing flow symmetry require an embedded suction system that has to be carefully adjusted.

The current experiment investigated the separated flows over a 2D wing with low AR in a range of α that forms a SC. To investigate the SC pattern and its asymmetry, the full span of the wing was characterized using several planar particle image velocimetry (PIV) measurements in planes that were parallel and close to the surface. A state-of-the-art 3D particle tracking velocimetry (3D-PTV) was used to characterize the SC topology beyond the near-wall planes of planar PIV. To carry out the 3D-PTV measurements over a large volume that captured the SC, a novel system was employed to generate larger tracer particles made of neutrally-buoyant helium-filled soap bubbles (HFSB). Finally, to identify the source of SC asymmetry and to obtain a symmetric SC, the present study investigated the improvement of the symmetry of the SC through the application of vane-type vortex generators (VGs) at different spanwise locations.

II. Experimental Setup

A. Wind Tunnel and Airfoil

The experiments were conducted in a two-story, closed-loop wind tunnel located at the University of Alberta. The test section followed a nozzle with a contraction ratio of 6.3:1 and had a cross-section of 1.2×2.4 m^2. The side and bottom walls of the wind tunnel had acrylic windows for optical access. A two-dimensional wing with NACA 4418 profile and a chord (c) of 975 mm, span (s) of 1190 mm, and AR of 1.2 was installed vertically in the wind tunnel. The wing was bounded by the wind tunnel walls from both spanwise ends. The TE section of the NACA 4418 airfoil, from 67% chord to the TE was modified into a straight surface. The modification was small and allowed the PIV measurement plane to stay parallel with the wing surface. A comparison between the original and modified NACA 4418 airfoils is demonstrated in Fig. 1. The TE section of the original NACA 4418 is shown in dashed line while the modified TE is shown with a solid line. Since the modification reduced the curvature, the separation location is

expected to be slightly downstream with respect to that of the original NACA 4418 airfoil. The modified section is also shown in black in the 3D view from Fig. 2. A full-span trip wire with 1 mm diameter was installed on the suction side of the airfoil at 20% chord using a thin tape to force a laminar-to-turbulent transition. The tripping step had a 2D cross-section resembling a bump with a height of approximately 1.1 mm. All the planar PIV measurements were carried out at Re_c of 672,000, which corresponds to freestream velocity of 10.5 m/s. Previous hotwire measurements recorded a freestream turbulence intensity of 0.43% at the velocity of 10.5 m/s [31]. Large-scale PIV measurements also showed that maximum variation in the mean velocity profile at the center of the test-section was approximately 0.61% [31]. For the 3D-PTV measurements, a slightly greater Re_c of 736,000, which corresponds to a freestream velocity of 11.5 m/s was used. This adjustment of the freestream velocity was needed to bring the SC back to the same streamwise location observed in the planar PIV measurements. The small displacement of the SC location between the two experiments was attributed to the presence of the HFSB system in the settling chamber. Both planar PIV and 3D-PTV measurements were carried out at an air temperature of 22 °C. At the freestream velocity of 11.5 m/s, the turbulence intensity was 0.56% when the HFSB system was installed in the settling chamber [31]. The maximum spatial deviation of the freestream velocity from the mean flow in the central region of the test section was 0.65% without the HFSB system, and 1.4% with the HFSB system installed in the settling chamber at the velocity of 11.5 m/s [31].

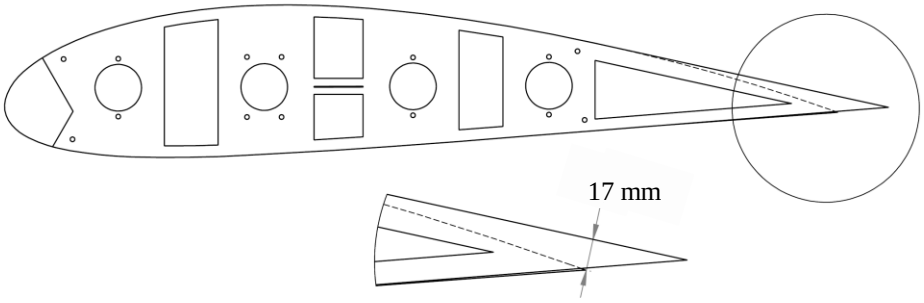

Fig. 1 Comparison between the original (dashed line) and modified (solid line) NACA 4418 airfoils.

The mean velocity profile of the BLs developed on the lower and upper walls of the empty test section was measured using planar PIV at the location of the airfoil. It was found that the BL thicknesses, δ_{99}, on the lower and upper walls were 70 mm and 146 mm, respectively. The thicker δ_{99} observed on the upper wall is potentially associated with the large gaps between the panels of the wind tunnel ceiling. The laminar-to-turbulent transition points may also be different on the upper and lower walls due to the closed-loop design of the wind tunnel and the asymmetry of the curved section upstream of the settling chamber.

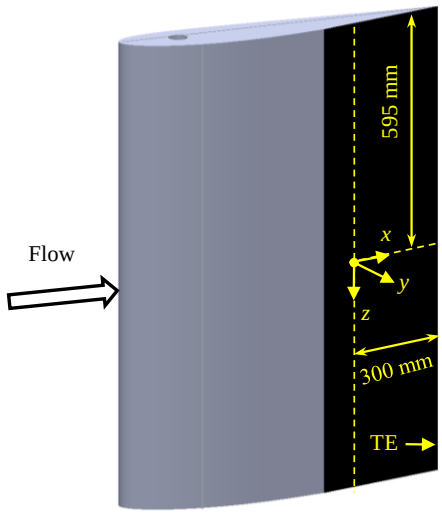

Fig. 2 The modified NACA 4418 airfoil and the coordinate system.

The maximum lift coefficient of the NACA 4418 airfoil occurs at approximately 14° [32]. The airfoil was tested here at α range of 9° to 11° in the pre-stall regime [32]. The α was increased in increments of 0.5° with an uncertainty of ±0.1° following α = 9.0°, 9.5°, 10.0°, 10.5°, 11°. An extra measurement was also carried out at α = 9.7°, where the SC appears. Tuft visualization was conducted to confirm that there was no large-scale separation close to the leading edge and that the flow separation only occurred close to the TE. The coordinate system used in the current experiment is demonstrated in Fig. 2. The streamwise, wall-normal, and spanwise directions are represented by x, y, and z, respectively. The origin of the coordinate system is at the midspan of the airfoil and 300 mm upstream of the TE. It is also at a wall-normal distance of 4 mm with respect to the airfoil surface. In this study, the y and z dimensions are normalized with s, and the x dimension is normalized with c. The TE is located at x/c = 0.3.

B. Vortex Generators

The current experiment investigated the usage of VGs to isolate the SC pattern from the separated flows on the spanwise ends of the airfoil. This approach aimed at enforcing an attached flow on the spanwise boundaries of the stall cell. Vane-type VGs were selected due to their simple geometry and effectiveness in controlling flow separation as shown by previous investigations [33-35]. The rectangular shape was shown to maximize the wall-normal momentum transport relative to the delta and trapezoidal type VGs [35]. The VGs used here were 3D printed using polylactic acid (PLA) in a Dremel 3D45 printer with a nozzle size of 0.2 mm.

As shown in the inset of Fig. 3a, the vanes of VG were arranged in pairs with an incidence angle, β, of 18° as suggested by Godard and Stanislas [36]. To produce large-scale streamwise vortices, also following Godard and

Stanislas [36], the height of the VGs, h, was scaled as $0.4\delta_{99}$. Here, δ_{99} is the BL thickness just upstream of the SC location which is approximately 26 mm based on measurements of Ma et al. [13]. Therefore, the height of VGs was 10 mm in the current experiment. The gap between the TEs of the vanes was fixed to 1h to minimize the decay of the vortex strength [37]. In addition, to ensure the strong vortices, the chord of the VGs was set to 6h [38].

According to the parametric study on vane-type VGs by Ashill et al. [39], the vortices produced by counter-rotating vanes evolve within a distance of 30h downstream of the VG, and then remain approximately constant between 30 to 50h downstream of the VG. Hence, the VGs were installed 40h (400 mm) upstream of the primary saddle point of the SC, which is around 25% of the chord. As it will be discussed in Sec. III., the asymmetry of the SC is associated with the secondary saddle and focus points that develop on the spanwise sides of the SC. Therefore, the spanwise VG locations were chosen according to the z locations of these secondary structures in an attempt to enforce a symmetric flow on the two spanwise sides of the SC. Three VG arrangements were selected as shown in Fig. 3: (a) two pairs of VGs at z/s = -0.41 and 0.26, (b) two additional VG pairs added at z/s = -0.32 and 0.42, (c) an additional VG pair was installed at z/s = -0.16. The VGs were investigated at an airfoil α of 9.7°, where the SC was first observed with increasing α.

a) b) c)

Fig. 3 The three arrangements of VG pairs used to enforce a symmetric flow around the SC.

C. Planar Particle Image Velocimetry

To investigate the effect of varying α and the VGs on the pattern of the separated flow, planar PIV measurements were conducted over the full span of the wing (1190 mm). A CCD camera (Imager ProX, LaVision GmbH) with a

sensor size of 2048 × 2048 pixels was used. Each pixel was 7.4 × 7.4 μm^2 and had a dynamic range of 14 bits. The camera was equipped with a Nikon lens with a focal length of f = 105 mm and an aperture of f / 5.6. The camera imaged a field-of-view (FOV) of 268 × 268 mm at a digital resolution of 0.13 mm/pixel. The camera location and the FOV are illustrated in Fig. 4a. The whole span (1190 × 268 mm) was scanned by moving the camera in the z direction as shown by multiple red rectangles in Fig. 4a. The combined FOV was stitched using vector mapping in DaVis 8.4 (LaVision GmbH). The stitched FOV was 268 mm × 1190 mm in the x and z directions, respectively. An Nd:YAG laser (Spectra-Physics, PIV 400) with a maximum power of 400 mJ per pulse at 532 nm wavelength was used to illuminate the measurement plane. The laser sheet was generated using a combination of spherical and cylindrical lenses and its thickness was kept smaller than 2 mm in the camera FOV. The laser sheet was parallel to the wing surface and at a wall-normal distance of 4 mm. The 4 mm distance minimized the glares formed in the images due to the reflection of the laser sheet. The flow was seeded using ~1 μm fog particles. Two independent sets of 500 double-frame images were collected for each measurement at a rate of 5 Hz with a laser-pulse separation of 200 μs. The signal-to-noise ratio (SNR) was improved by subtracting the ensemble minimum of the image intensities from each image, followed by normalization using the average image intensity. The double-frame images were cross-correlated in DaVis 8.4 (LaVision GmbH) using a multi-pass algorithm with a final interrogation window of 32 × 32 pixels (4.2 × 4.2 mm^2) at 75% overlap. Universal outlier detection was applied in the post-processing procedure to remove the spurious vectors [40]. The uncertainty of planar PIV measurements is estimated to be approximately 0.1 pixels [41]. Therefore, using the digital resolution (0.13 mm/pix) and separation time between the two laser pulses (200 μs), the error in the velocity vector is 0.063 m/s ($6\times10^{-3}U_\infty$). In addition, evaluations of displacement histograms did not show any evidence of peak-locking. The statistical convergence of the planar PIV measurements was examined for both U and W components. The results showed that the arithmetic mean of both U and W converged to the expected mean after about 500 vector fields. The maximum variation of the arithmetic mean was approximately 2% when the number of planar-PIV vectors increased from 900 to 1,000.

D. Three-dimensional Particle Tracking Velocimetry

To study the 3D topology of the SC, a large-scale 3D-PTV measurement was conducted. Relative to the planar PIV, the 3D-PTV measurement covered a smaller spanwise extent but provided a volumetric measurement. The 3D-PTV experiment was conducted at α of 9.7° and covered the midspan of the airfoil as demonstrated in Fig. 4b. The imaging system consisted of four high-speed cameras (v611 phantom). Each camera had a sensor size of 1280 × 800

pixels, with a pixel dimension of 20 × 20 μm^2. Nikon lenses with a focal length of f =105 mm were set to an aperture size of f / 11 to obtain a depth-of-focus of approximately 100 mm. An angle of approximately 40° was kept between the opposite cameras. Sheimpflug adapters were used to align the depth-of-focus of the cameras and the measurement volume. The latter was illuminated by a high-speed Nd:YLF laser (Photonics Industries, DM20-527DH) with 20 mJ per pulse at 4 kHz. The laser beam was expanded by a combination of two cylindrical lenses. To obtain a rectangular cross-section, the laser beam was cropped at four edges. The measurement volume was 260 × 100 × 380 mm^3 in the x, y, and z directions, respectively, which is equivalent to 807 × 310 × 1180 pixels. The initial calibration of the cameras was obtained by fitting a third-order polynomial on an image recorded of a 3D calibration plate (Type 22, LaVision GmbH). The self-calibration algorithm was then applied to reduce the root-mean-square of image distortion residual to 0.1 pixels [42].

Since the laser energy was expanded over a large volume, it was essential to use large tracers that scatter sufficient light. For this reason, an in-house seeding system was employed to generate neutrally buoyant helium-filled soap bubbles (HFSB) with a mean diameter of approximately 0.5 mm [43]. The nozzles that generated HFSB bubbles were installed on a structure shown in Fig. 5a and b. The structure had 4 modular ducts with 12 nozzles installed in each duct (a total of 48 nozzles). The nozzles pointed downward and were installed in a staggered pattern on the top plate of the duct. The ducts had a thin wall of 3 mm thickness. The structure had a supporting base with NACA 0012 profiles. The airfoils had a thickness of ~15 mm to reduce the flow blockage and downstream disturbances. The HFSB structure was placed in the settling chamber, upstream of the contraction section, as seen in Fig. 5c. The blockage of the HFSB structure increased the freestream turbulence intensity by approximately 0.1% and increased the non-uniformity of the mean flow by 0.8% [31]. This resulted in a displacement of the SC towards the TE, which was compensated by increasing the freestream velocity to 11.5 m/s for the 3D-PTV measurements. The disturbances induced by the HFSB system can be further reduced potentially by reducing the cross-section of the supporting structure, or installing the HFSB system upstream of the wind tunnel screens. The latter option may reduce the number of the bubbles that reach the test section and requires frequent maintenance of the wind tunnel screens. The HFSB system was only employed for the 3D-PTV measurements, and was removed from the test section during the planar-PIV measurements.

In total, 10,800 images were recorded by each camera at an acquisition frequency of 4 kHz. Similar to the planar PIV, the ensemble minimum intensity was subtracted from each image and an image normalization using the ensemble

average was conducted. An optical transfer function was calculated for the iterative particle reconstruction and particle shaking processes of the shake-the-box (STB) algorithm [44, 45], conducted in DaVis 8.4 (LaVision GmbH). For the STB process, the maximum allowable particle shift was set to 15 pixels. On average, 3,500 particles were detected per image, which resulted in a particle image density of approximately 0.003 particle per pixel (ppp). The particle image density was limited by the number of bubbles generated by the HFSB system and their dispersion in the wind tunnel. The particle image density was well below the 0.075 ppp upper threshold of the STB algorithm [45]. The 3D-PTV algorithm detected 2000 tracks per image. A second-order polynomial with a kernel of 2.8 ms (11 time steps) was applied to the particle tracks. The velocity measurements from all the images were binned into a grid with a final window of 48 × 48 × 48 voxels (15 × 15 × 15 mm^3) at 75% overlap. Approximately 8,000 particle tracks were found in each bin. The uncertainty of the 3D-PTV measurement is estimated to be 0.1, 0.2, and 0.1 pixels in the *x*, *y*, and *z* directions based on the analysis of Ebrahimian et al. [46] and Rowin and Ghaemi [47]. Here, the largest uncertainty of 0.2 pixel corresponds to the out-of-plane direction of the 3D-PTV system. Using the digital resolution of 0.32 mm/pixel and acquisition frequency of 4 kHz, the velocity uncertainties are 0.13 m/s ($0.011U_\infty$), 0.26 m/s ($0.023U_\infty$), and 0.13 m/s ($0.011U_\infty$) in the *x*, *y*, and *z* directions, respectively. The statistical convergence of the mean of the velocity components obtained from 3D-PTV was investigated by calculating the arithmetic mean values using different number of detected particles. The results showed that the arithmetic mean calculated based on 90% of the total number of particles was no more than 3% different with respect to the mean value calculated using the total number of particles.

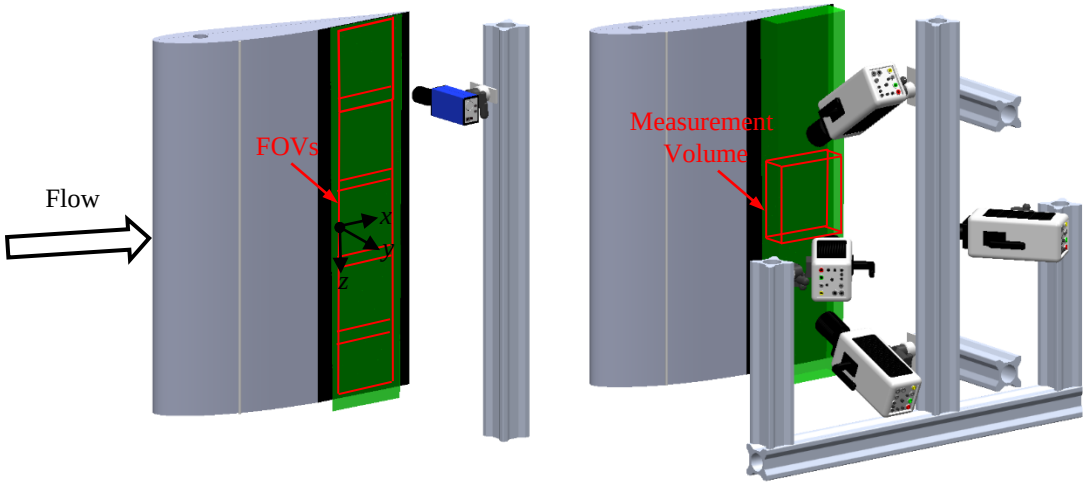

a) b)

Fig. 4 Schematics of the experimental setup for a) planar PIV and b) 3D-PTV measurements.

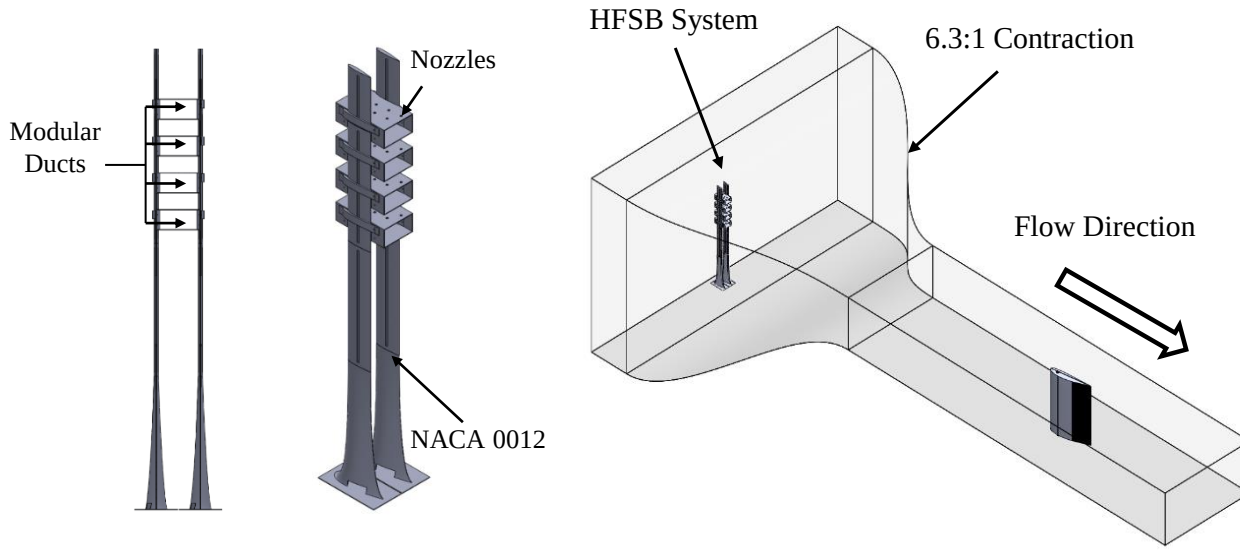

a) b) c)

Fig. 5 The a) front and b) isometric views of the HFSB system. c) The position of the HFSB system in the wind tunnel.

III. Results

To study the effect of α on the SC pattern, the flow streamlines obtain from the planar PIV measurements of mean velocity are investigated in Sec. III.A. The planar analysis is followed by the investigation of the 3D structure of the SC using the large-scale 3D-PTV in Sec. III.B. Finally, the spanwise asymmetry in the SC pattern is addressed by deploying vane-type VGs in Sec. III.C.

A. The Effect of Angle of Attack on Stall Cell

The flow streamlines over the full span of the wing for different α are plotted in Fig. 6. The upper and lower wind tunnel walls are at z/s = -0.5 and 0.5, respectively. The measurement domain covers the area close to the TE, with the TE located at x/c = 0.3. The saddle points and foci are labeled with the cross sign (×), and plus sign (+), respectively. The separation lines are also highlighted with dashed lines. Note that the HFSB apparatus or VGs were not installed during the planar-PIV measurement reported in this section.

The streamline pattern at α = 9° in Fig. 6a shows a large recirculating vortex (labeled as A) near the upper spanwise end (z/s = -0.5). The corresponding focus point of this vortex is at (x/c, z/s) = (0.21, -0.41). Near the midspan of the wing, a saddle point is observed at (x/c, z/s) = (0.21, -0.05), and a focus point is located close to the TE at (x/c, z/s) = (0.25, -0.11). A short separation line also occurs in the mid-span region, crossing through the saddle point. No large recirculating flow is visible near the bottom end of the span at z/s = 0.5. Therefore, the corner flows at the two spanwise

ends of the wing are dissimilar although the wing and wind tunnel walls are symmetric (within the manufacturing tolerances). As noted in Sec. II.A. the turbulent BL thickness on the upper wind tunnel wall (z/s = -0.5) is approximately twice of that on the lower wall (z/s = 0.5). The smaller flow momentum on the upper wall contributes to the formation of vortex A on the upper end of the airfoil. When α is increased to 9.5° in Fig. 6b, the focus point A moves slightly to (x/c, z/s) = (0.20, -0.40), and the associated recirculating region is enlarged. At the midspan, the separation line extends and covers a larger spanwise domain. The separation line undulates in the spanwise direction and crosses two saddle points at (x/c, z/s) = (0.21, -0.01) and (0.17, 0.09). There are also three foci at (x/c, z/s) = (0.24, -0.11), (0.18, 0.03), and (0.23, 0.31). However, no SC pattern is apparent at this α.

As α further increases to 9.7° in Fig. 6c, the focus A moves farther upstream to (x/c, z/s) = (0.18, -0.42). A SC is observed with a saddle point M at (0.05, 0.05) and two counter-rotating foci indicated as B and C. The combination forms a mushroom-shape separation line. An adjacent secondary vortex D is also seen at (x/c, z/s) = (0.21, 0.27), and a secondary saddle point N forms at (x/c, z/s) = (0.20, 0.19). The lower spanwise section from z/s = 0.35 to 0.5 still shows no sign of flow separation or a recirculating region. The SC is formed here for a wing with a low AR of 1.2 relative to the previous investigations that observed SC over wings with higher ARs [10, 15].

For α of 10° in Fig. 6d, the primary saddle point M and the focus point B remain at the same location while the focus C moves slightly upstream and down to (x/c, z/s) = (0.13, 0.10). The secondary saddle point N also moves upstream and down to (x/c, z/s) = (0.17, 0.19). The curvature of the separation line connecting B and M also increases, and the reversed flow area becomes larger. Foci A and D remain in their former locations. The distance between the two foci of the SC in the current investigation at α of 10° is 0.21s. This is close to the SC width of 0.26s observed in the numerical simulation of flow over a 2D wing with AR = 2 at α = 10° and Re_c of 8.7×10^5 [12]. The SC observed by Dell'Orso and Amitay [8] for a wing with AR = 4 at α = 16.5° and Re_c of 4.11×10^5 had a larger width of 0.43s. This larger spacing with respect to the current investigation is potentially due to the larger α and AR. A larger α can result in a larger separation zone while a larger AR also allows the SC to expand in the z direction without being confined by the corner flows.

In Fig. 6e, corresponding to α of 10.5°, the separation front moves farther upstream. As a result, the primary saddle point M and part of the separation line move out of the measurement field. The focus point C moves away from focus B, and the SC widens. A new saddle point also appears at (x/c, z/s) = (0.26, -0.24). With a further increase of α to 11° in Fig. 6f, the focus point A is pushed downstream to (x/c, z/s) = (0.25, -0.41), and the SC has a larger recirculating

region. The two foci B and C move to (x/c, z/s) = (0.10, -0.13) and (0.05, 0.19), resulting in a larger spanwise spacing of 0.32s. The adjacent focus point D and the secondary saddle point N no longer exist. It is conjectured that the expansion of SC accelerated the flow around the SC and removed the secondary focus and saddle points (N and D in Fig. 6e). Note that the saddle point between foci A and B is no longer visible when α reaches 11°. The topology for α higher than 11° was not investigated since the main flow features shifted outside of the measurement domain that covered the flat TE section.

The investigation of the streamlines showed that the flow separation pattern is sensitive to the variation of α. At the early stages of the TE separation (α = 9°), the flow along the span of the airfoil consisted of small, isolated pockets of backflow. With a slight increase of α to 9.5°, the isolated pockets merged forming an undulated separation front with multiple foci and saddle points. When α increased further to 9.7°, an asymmetric SC pattern formed. A secondary saddle point and a secondary focus structure also appeared on one side of the SC, forming an asymmetric pattern with respect to the midspan. The flows at the two spanwise ends of the wing were not symmetric; a corner vortex with large backflow existed at one side while the flow was attached on the other spanwise end of the wing. This asymmetric flow pattern can be caused by imperfections in the experimental apparatus that are difficult to avoid. In particular, the difference in the BLs on the wind tunnel walls at the two spanwise ends of the wing produces the dissimilar corner flows observed in Fig. 6. Similar asymmetric flow patterns were also observed in the tuft visualization by Broeren and Bragg [11] and the oil-flow visualization by Dell'Orso and Amitay [8]: a corner vortex with a reverse flow region was present only at one of the spanwise ends and persisted with increasing α. In the current investigation, as a result of the blockage caused by the corner vortex of the upper spanwise end, the flow between the corner vortex and SC accelerates and remains attached at higher α. In contrast, between the other spanwise end of the wing and the SC, a short separation line with a focus point D and a saddle point N forms. The observation suggests the absence of a corner vortex at z/s = 0.5 may be responsible for the existence of the saddle point N and focus point D on the lower side of the SC. Further increase of α to 10.5° expands the SC in the spanwise direction. When the SC covers approximately 50% of the span (α = 11°), the secondary saddle point and focus point disappear. In addition, the reverse flow region observed at the upper spanwise corner of the wing appears to weaken: the saddle point observed in Fig. 6e is not visible anymore in Fig. 6f as the corner vortex A moves more downstream and the associated reverse flow area is smaller within the FOV. Based on these results, one can predict that the SC will continue to expand with the increasing α and will cover most

of the wingspan. Note that it is also rare to observe a SC at a low AR of 1.2 since most of the studies of the SC were conducted on airfoils with larger AR [7-17, 19-24].

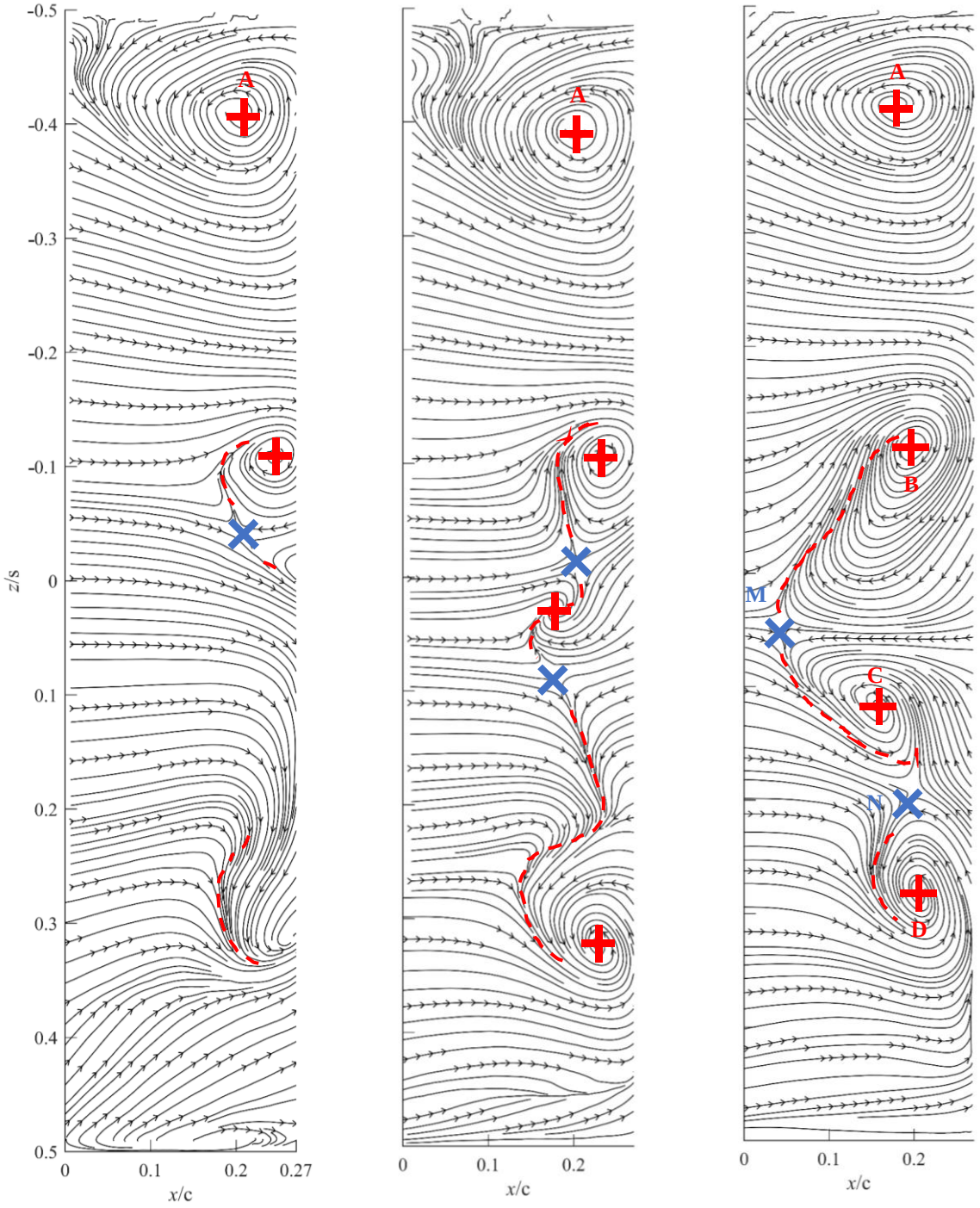

a) b) c)

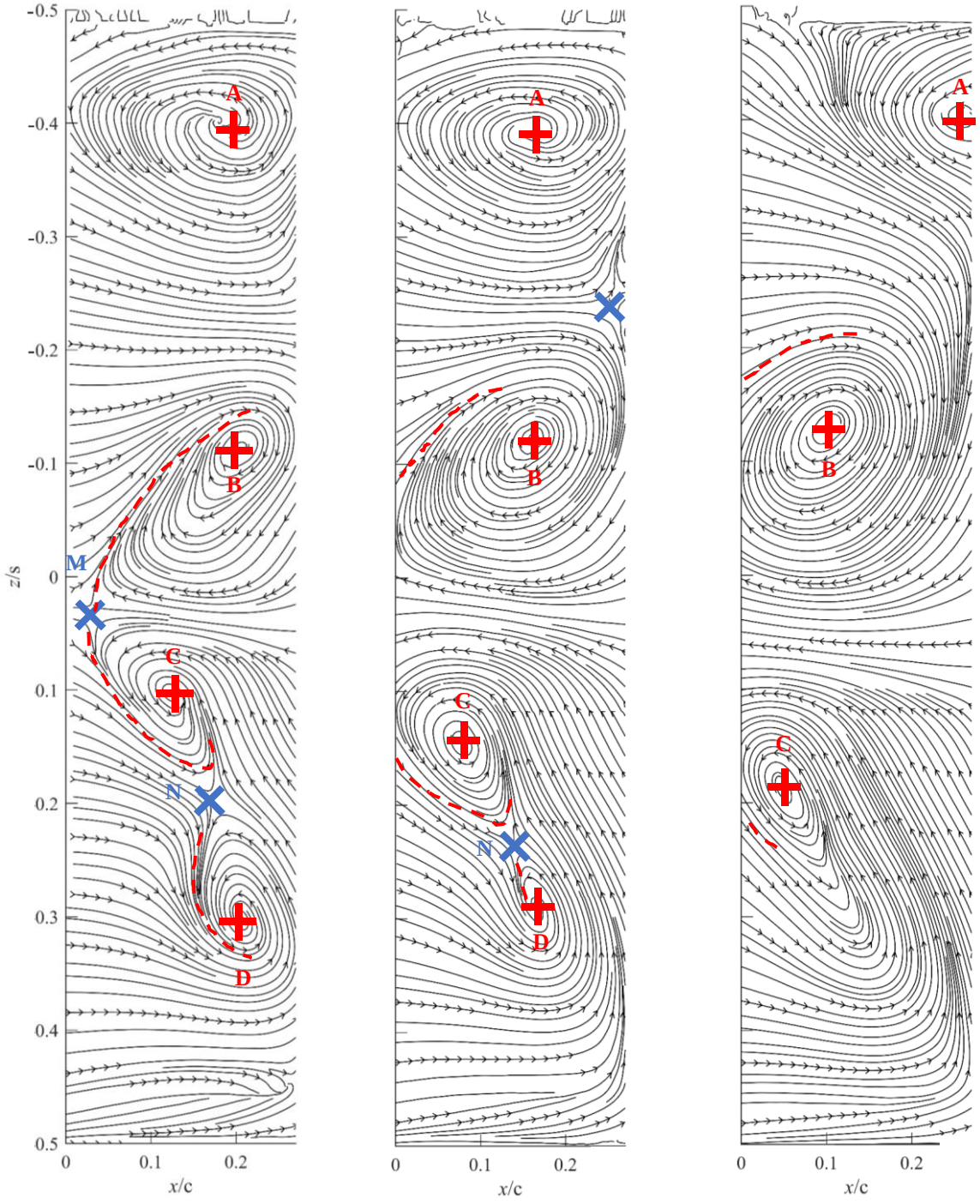

d) e) f)

Fig. 6 Streamline pattern over the airfoil at α of a) 9°, b) 9.5°, c) 9.7°, d) 10°, e) 10.5° and f) 11°.

B. Three-dimensional Characterization of Separation Bubble

The 3D-PTV was performed to obtain the 3D topology of the SC. The mean velocity fields from the 3D-PTV are presented in 3 planes in Fig. 7: a near-wall *x*-*z* plane ($y/s = 4 \times 10^{-3}$), a *x*-*y* plane at $z/s = -0.02$, and a *y*-*z* plane at $x/c = 0.2$. The figure shows the 2D streamlines with contours of normalized streamwise velocity, $\langle U \rangle / U_\infty$, in the background. The streamlines of the *x*-*z* view show the mushroom-shape separation front and two counter-rotating foci of the SC. The SC is relatively symmetric in the spanwise direction. The *x*-*y* plane shows that the maximum height of the separation bubble, characterized by $\langle U \rangle / U_\infty = 0$, is about $0.015s$ ($0.018c$) at $x/c = 0.22c$ (~$0.08c$ upstream of the TE). The short wall-normal height of the separation bubble leaves little space for the foci structures to develop in the wall-normal direction. This is confirmed in Fig. 8, where *x*-*z* planes at higher wall-normal locations of $y/s = 7.5 \times 10^{-3}$, 0.01, and 0.015 are presented. As observed in Fig.8, the foci structure quickly disappears with increasing y/s when approaching the boundaries of the separation bubble. The counter-rotating vortices are not visible anymore at $y/s = 0.015$. This shallow separation bubble is consistent with the pre-stall condition of the airfoil. For example, Dell'Orso and Amitay [8] observed a SC with a wall-normal height of $0.3c$ at $0.12c$ upstream of the TE at α of 16.5°. The thicker separation bubble in the investigation of Dell'Orso and Amitay [8] is associated with the larger α and the corresponding post-stall regime. As it is observed in the *y*-*z* plane of Fig 6, the height of the separation bubble increases with increasing x/c.

The streamlines in the *y*-*z* plane of Fig. 7 do not show any streamwise vortex. To confirm the absence of streamwise vortices, additional *y*-*z* planes are shown at different streamwise locations in Fig. 9. At $x/c = 0.15$, upstream to the two counter-rotating foci, a 3D node of detachment-type is observed. The streamlines show that the flow moves away radially from the node and departs from the wall. When viewing the *y*-*z* planes farther downstream at $x/c = 0.17$ and 0.18, where the two foci are present, the node is no longer visible. At these two planes, a large-scale wall-normal motion of the flow away from the surface is seen, while the streamlines are slightly skewed towards the positive *z* direction. The most downstream *y*-*z* plane at $x/c = 0.19$ also shows no evidence of a streamwise vortex pair. In this *y*-*z* plane, an upward flow with a half-saddle structure is observed approximately at $z/s = 0$.

The 3D visualization of the SC did not show any evidence of strong streamwise vortices at the pre-stall condition in the current experiment. The streamwise-spanwise planes showed that the wall-normal vortices weaken and disappear at the boundary of the separation bubble, before tilting in the freestream direction. This observation agrees with the results of Dell'Orso and Amitay [17] which was carried out for an airfoil at near stall condition.

The mean 3D flow field of the separated flow is demonstrated in Fig. 10. The boundaries of the separation bubble are visualized using an iso-surface of $\langle U \rangle = 0$, colored by transparent green. The flow motion is represented using colored 3D streamlines. The streamline sections with forward-moving flow (positive U) are colored in red, while the backward-moving sections are shown in blue. Short segments of white streamlines are used to represents near-zero streamwise velocity, which coincide with the boundary of the separation bubble. The blue color of the streamlines with spiral motion shows that two large vortices are confined within the separation bubble, which agrees with the streamline pattern of x-z planes in Fig. 7 and 8. The streamlines illustrate that most of the flow within the separation bubble is brought into the bubble by the backflow induced between the two counter-rotating foci. The flow within the separation bubbles moves upstream against the freestream flow forming the front separation line.

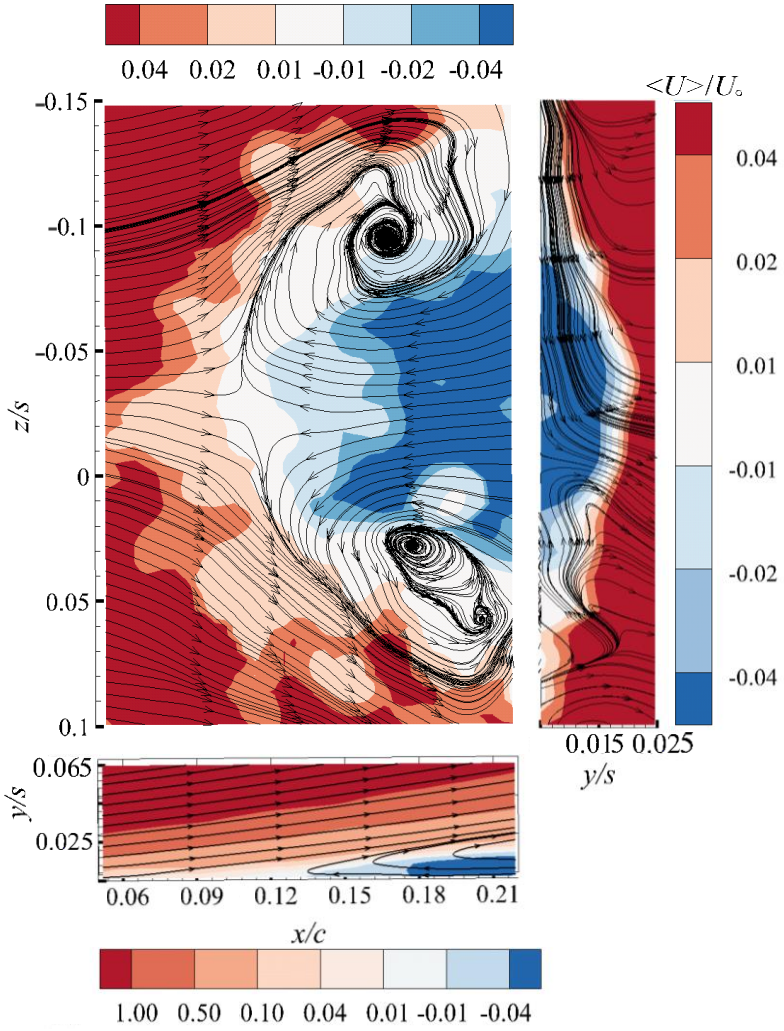

Fig. 7 Visualization of the SC in a x-z plane at $y/s = 4 \times 10^{-3}$, a x-y plane at $z/s = 0.02$ and a y-z plane at $x/c = 0.22$.

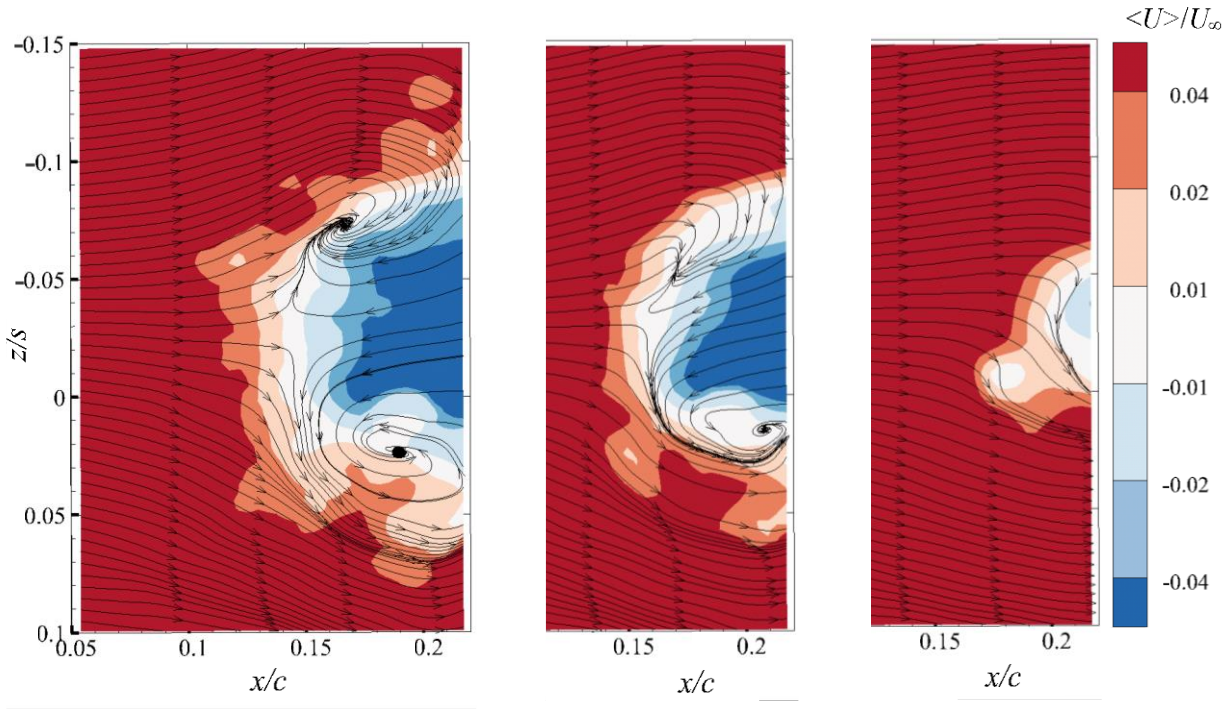

a) b) c)

Fig. 8 The velocity field in *x*-*z* planes at a) *y*/*s* = 0.0075, b) *y*/*s* = 0.01, and c) *y*/*s* = 0.015.

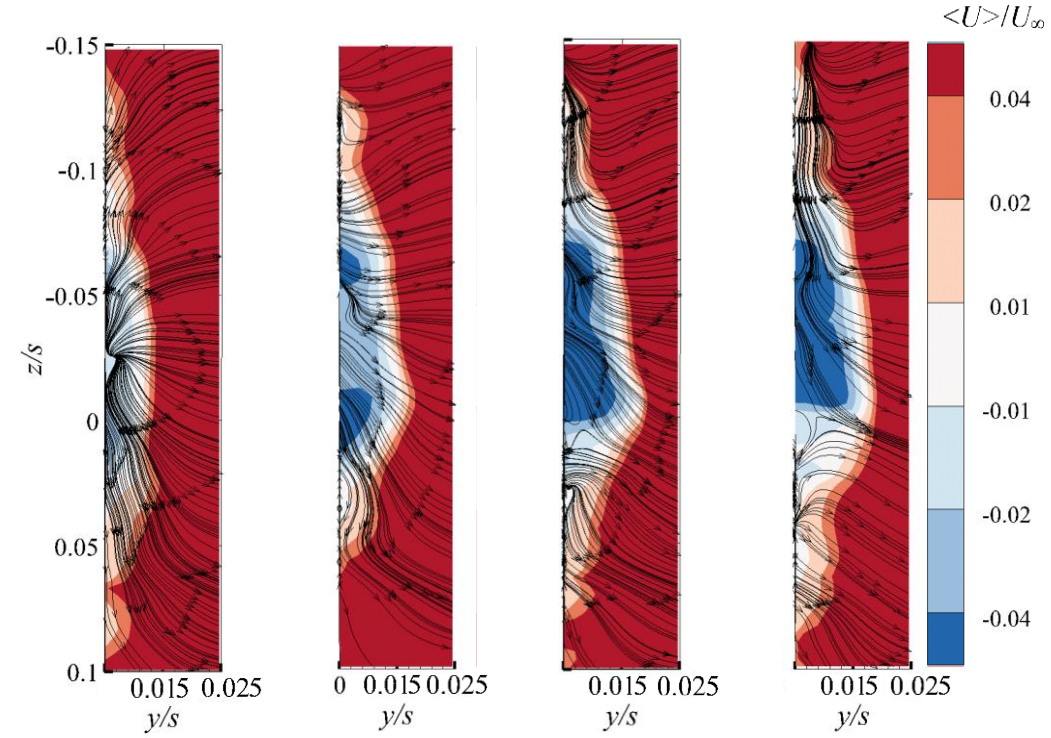

a) b) c) d)

Fig. 9 The velocity field in *y*-*z* plane at a) *x*/*c* = 0.15, b) *x*/*c* = 0.17, and c) *x*/*c* = 0.18, and *x*/*c* = 0.19.

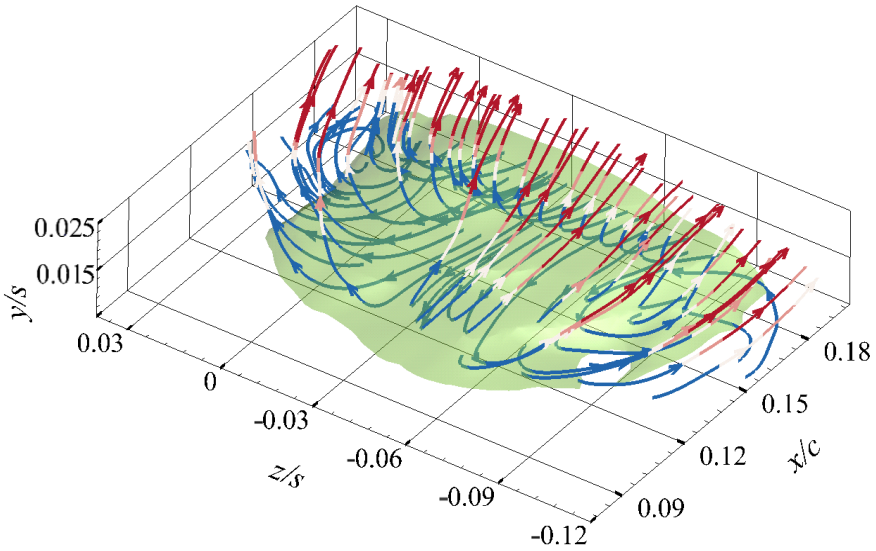

Fig. 10 The 3D streamlines of the SC. The green iso-surface shows $\langle U \rangle / U_\infty = 0$. The blue, white, and red streamlines indicate negative, zero, and positive streamwise velocity (backward-to-forward flow).

C. Application of Vortex Generators

The streamline patterns of the SC after applying the VG combinations are presented in Fig. 11. The green v-shape marks demonstrate the spanwise location of the VGs. Note that the streamwise location of the VGs is at 0.25*c* downstream of the leading-edge, which is outside of the domain shown in Fig. 11. To characterize the asymmetry of the SC, the parameter *S* is defined as the $|l_B - l_C| / |l_B + l_C|$. Here, l_B and l_C represent the distance between the saddle point M and foci B and C in the *z* direction, respectively. For a symmetric SC, a *S* value of zero is expected.

The streamline pattern of Fig. 6c showed that foci A and D contributed to in the asymmetry of the SC. This is also observed by the large *S* value of 0.39 for this flow field. Therefore, as shown in Fig. 11a, two pairs of VGs are installed at z/s = -0.41 and 0.26 to prevent the formation of foci A and D. The results in Fig. 11a show a significant improvement in the spanwise symmetry of the SC by applying the VGs, which resulted in *S* value of 0.26. However, a slight spanwise asymmetry persists, such that, in the *z* direction, the upper focus point B is farther from the primary saddle point M relative to the distance between the saddle point M and focus C. The additional momentum brought in by applying the VG at z/s = -0.41 slightly pushed the focus point A downstream. The VG installed at z/s = 0.26 removed the focus point D and saddle point N that were presented in Fig. 6c. A recirculating region is created near z/s = 0.5 at the lower spanwise end of the wing.

To further improve the symmetry of the SC pattern, two additional pairs of VGs are added at z/s = -0.32 and z/s = 0.42 as seen in Fig. 11b. The saddle point M makes a small downstream movement of 0.01*c*. The two foci barely move. Hence, the new VGs provides little improvement in terms of SC symmetry. In particular, the VG installed at

z/s = -0.32 does not affect the high-speed flow formed between the recirculating flow at the upper corner of the wing and the SC. The VG at z/s = 0.42 removes a part of the backward flow near the lower wind tunnel wall and confines it to a small spanwise region. However, this has a negligible effect on the SC, the value of S changed from 0.26 to 0.28 with the addition of the VGs, which suggests that the small recirculating flow at the lower spanwise end did not affect the SC.

One more attempt is conducted to enhance the symmetry of the SC by adding a pair of VGs at z/s = -0.16, and the result is shown in Fig. 11c. The added VG increases the streamwise momentum of the flow and shifts the focus point B in the positive z direction. Note that the two foci B and C are drawn closer together, and are relocated to (x/c, z/s) = (0.18, -0.04) and (0.19, 0.15). The corner vortex near the top end of the span at z/s = -0.5 still exists. The VGs induced a symmetric boundary on the two spanwise sides of the SC and formed a symmetric SC with a small S value of 0.05. The investigation shows that VGs can effectively reduce the interference of the corner flows with the flow at the mid-span of the wing and remove the undesired secondary flow structures. This technique can be used for generating SCs that are isolated from the corner flows at the spanwise ends of the airfoil, improving the repeatability of the experiments.

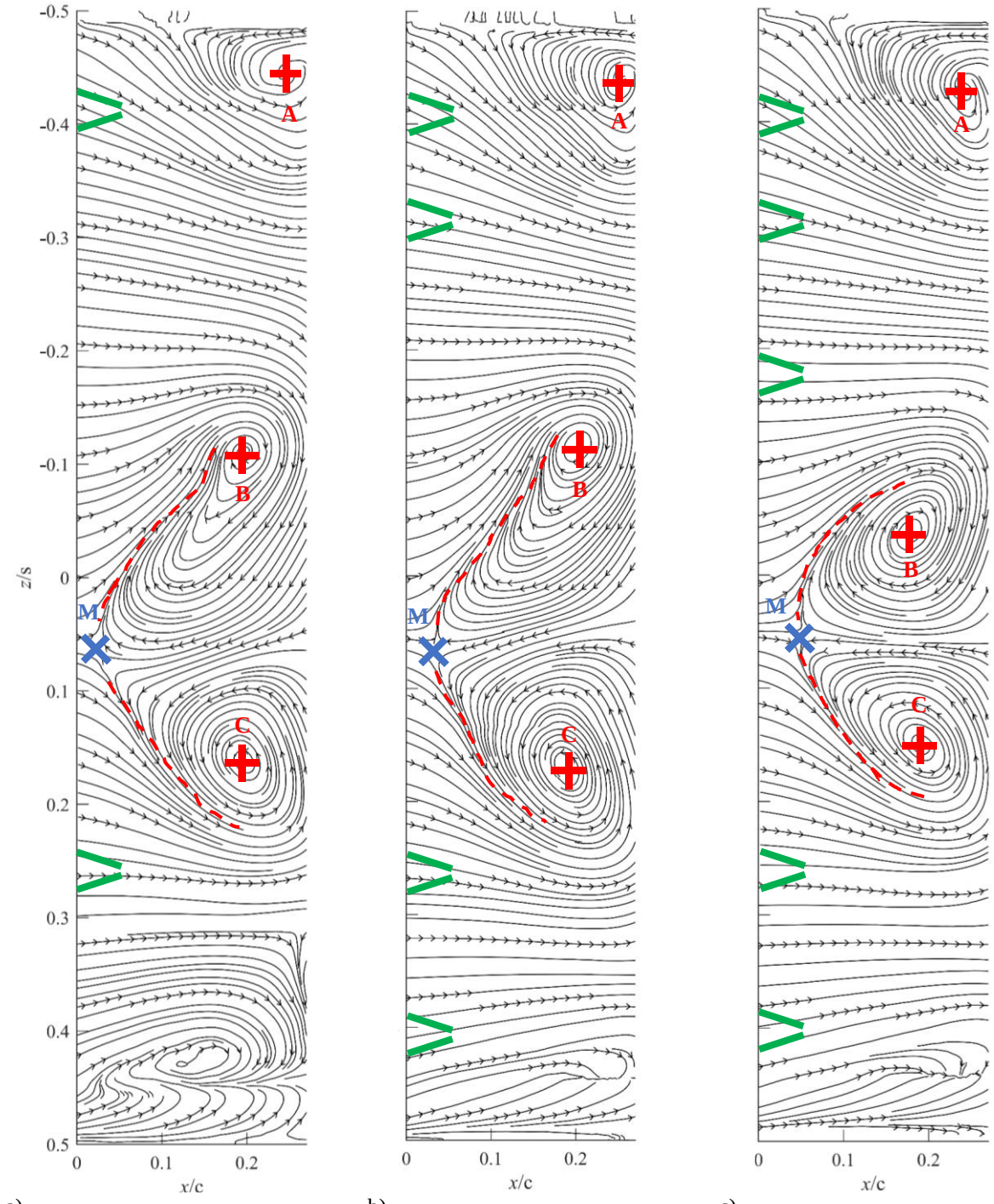

a) b) c)

Fig. 11 The effect of VG arrangements on the streamlines at α of 9.7°.

IV.Conclusion

The current investigation characterized the SC pattern over a 2D wing with NACA 4418 airfoil at pre-stall conditions. The flow streamlines over the full span of the 2D wing at various α was measured using multiple planar-PIV measurements. The measurements showed a recirculating vortex near one of the spanwise ends of the wing and an attached forward flow near the other spanwise end of the wing. This asymmetry was likely due to the dissimilar BLs developed along the upper and lower wind tunnel walls. At the lowest α of 9°, isolated pockets of backflow were observed. With increasing α to 9.5°, the isolated zones merged and formed an undulating separation front with two saddles and three foci structures. With a slight increase of α to 9.7°, an asymmetric SC formed. A secondary saddle and vortex structure also formed between the SC and the spanwise end of the wing that had an attached flow. With further increase of α, the separation line shifted upstream and the two counter-rotating foci within the SC departed away from each other. This resulted in a wider SC and a larger separated flow region. At α = 11°, the SC covered more than half of the wingspan, and the secondary saddle and vortex structures disappeared. In the present study, the SC formed at a low AR of 1.2, which was not commonly seen in the literatures. Previous studies were mostly conducted on airfoils with greater AR. In addition, only one SC was observed within the tested α, which is attributed to the pre-stall regime and the low AR of the wing.

The state-of-the-art 3D-PTV measurements were performed over a volumetric domain that covered the entire separation bubble. The 3D measurement over such a large volume of 260×100×380 mm^3 became feasible by applying helium-filled soap bubbles as neutrally-buoyant tracers. The 3D-PTV measurements showed that the SC formed a shallow separation bubble at α of 9.7°. The two counter-rotating vortices of the SC only extended a short distance in the wall-normal direction which was up to the boundary of the separation bubble. The 3D streamlines of the mean flow did not show any evidence of streamwise vortices. The 3D streamlines showed that the upstream flow enters the two foci structures from the outer bounds of the SC, and then transported away in the wall-normal direction.

Vane-type vortex generators (VGs) were deployed as a simple technique to enhance the symmetry of the SC pattern. It was shown that by installing the VGs in the outer bounds of the SC, the symmetry-breaking secondary structures can be removed. As a result, similar attached flows were introduced on the two spanwise sides of the SC, which formed a symmetric SC. The symmetric SC pattern can be used as a benchmark flow for fundamental investigation and control of separated flows.

Acknowledgments

This funding for this project was provided by Future Energy Systems at the University of Alberta (Grant number T14-P05).

References

[1] Sears, W. R., and Telionis, D. P., "Boundary-layer Separation in Unsteady Flow," *SIAM Journal on Applied Mathematics*, Vol. 28, No. 1, 1975, pp. 215-235.
doi: 10.1137/0128018

[2] Shen, S. F., "Unsteady Separation According to the Boundary-layer Equation," *Advances in Applied Mechanics*, Vol. 18, 1979, pp. 177-220.
doi: 10.1016/S0065-2156(08)70267-9

[3] Simpson, R. L., "A Review of Some Phenomena in Turbulent Flow Separation," *Journal of Fluids Engineering*, Vol. 103, No. 4, 1981, pp. 520-533.
doi: 10.1115/1.3241761

[4] Schneck, D. J., and Ostrach, S., "Pulsatile Blood Flow in a Diverging Circular Channel," F.T.A.S./TR-73-86, 1973.

[5] Tobak, M., and Peake, D. J., "Topology of Three-dimensional Separated Flows," *Annual review of fluid mechanics*, Vol. 14, No. 1, 1982, pp. 61-85.
doi: 10.1146/annurev.fl.14.010182.000425

[6] Délery, J., *Three-dimensional Separated Flow Topology: Critical Points, Separation Lines and Vortical Structures*, 1st ed., John Wiley and Sons, 2013, pp. 9-14.

[7] Moss, G.F., and Murdin, P. P., "Two-Dimensional Low-Speed Tunnel Tests on the NACA 0012 Section Including Measurements Made During Pitching Oscillations at the Stall," Her Majesty's Stationary Office, Aeronautical Research Council, CP No. 1145, London, May 1971.

[8] Dell'Orso, H., and Amitay, M., "Parametric Investigation of Stall Cell Formation on a NACA 0015 Airfoil," *AIAA Journal*, Vol. 56, No. 8, 2018, pp. 3216-3228.
doi: 10.2514/1.J056850

[9] Weihs, D., and Katz, J., "Cellular Patterns in Poststall Flow Over Unswept Wings," *AIAA Journal*, Vol. 21, No. 12), 1983, pp. 1757-1759.
doi: 10.2514/3.8321

[10] Yon, S. A., and Katz, J., "Study of the Unsteady Flow Features on a Stalled Wing," *AIAA journal*, Vol. 36, No. 3, 1998, pp. 305-312.

doi: 10.2514/2.372

[11] Broeren, A. P., and Bragg, M. B., "Spanwise Variation in the Unsteady Stalling Flowfields of Two-dimensional Airfoil Models," *AIAA Journal*, Vol. 39, No. 9, 2001, pp. 1641-1651.

doi: 10.2514/2.1501

[12] Manolesos, M., and Voutsinas, S. G., "Study of a Stall Cell Using Stereo Particle Image Velocimetry," *Physics of Fluids*, Vol. 26, No. 4, 2014, pp. 045101.

doi: 10.1063/1.4869726

[13] Ma, A., Gibeau, B., and Ghaemi, S., "Time-resolved Topology of Turbulent Boundary Layer Separation Over the Trailing-edge of an Airfoil," *Journal of Fluid Mechanics*, Vol. 891, A1, 2020.

doi: 10.1017/jfm.2020.106

[14] Boiko, A. V., Dovgal, A. V., Zanin, B. Y., and Kozlov, V. V., "Three-dimensional Structure of Separated Flows on Wings," *Thermophysics and Aeromechanics*, Vol, 3, No. 1, 1996, pp. 1-13.

[15] Winkelmann, A., "An Experimental Study of Separated Flow on a Finite Wing," *AIAA Journal, 7th Atmospheric Flight Mechanics Conference*, 1981, pp. 1882.

doi: 10.2514/6.1981-1882

[16] Winkelman, A. E., and Barlow, J. B., "Flow Field Model for a Rectangular Planform Wing Beyond Stall," *AIAA Journal*, Vol. 18,No. 8, 1980, pp. 1006-1008.

doi: 10.2514/3.50846

[17] Dell'Orso, H., Tuna, B. A., and Amitay, M., "Measurement of Three-dimensional Stall Cells on a Two-dimensional NACA0015 Airfoil," *AIAA Journal*, Vol. 54, No. 12, 2016, pp. 3872-3883.

doi: 10.2514/1.J054848

[18] Crow, S. C., "Stability Theory for a Pair of Trailing Vortices," *AIAA journal*, Vol. 8, No. 12, 1970, pp. 2172-2179.

doi: 10.2514/3.6083

[19] Manolesos, M., and Voutsinas, S. G., "Geometrical Characterization of Stall Cells on Rectangular Wings," *Wind Energy*, Vol. 17, No. 9, 2014, pp. 1301-1314.

doi: 10.1002/we.1634

[20] Sivaneri, V., and Amitay, M., "Formation of Three-dimensional Stall Cells on Two-Dimensional Airfoils," *Proceedings of the 55th Annual Israle Annual Conference on Aerospace Sciences*, Haifa, Israel, 2014, pp. 1-10.

[21] DeMauro, E.P., Dell'Orso, H., Sivaneri, V., Tuna, B. A., and Amitay, M., "Measurements of 3-D Stall Cells on 2-D Airfoils," *45th AIAA Fluid Dynamics Conference*, AIAA Paper 2015-2633, 2015.
doi:10.2514/6.2015-2633

[22] Dell'Orso, H., Chan, W., and Amitay, M., "Induced Stall Cells on a NACA0015 Airfoil Using Passive and Active Trips," *8th AIAA Flow Control Conference*, AIAA Paper 2016-3621, 2016.
doi:10.2514/6.2016-3621

[23] Esfahani, A., Webb, N., and Samimy, M., "Stall Cell Formation Over a Post-Stall Airfoil: Effects of Active Perturbations Using Plasma Actuators," *Experiments in Fluids,* Vol. 59, No., 132, 2018.
doi: 10.1007/s00348-018-2588-y

[24] Sarlak, H., Frèrre, A., Mikkelsen, R., and Sørensen, J. N., "Experimental Investigation of Static Stall Hysteresis and 3-Dimensional Flow Structures for an Nrel S826 Wing Section of Finite Span," *Energies*, Vol. 11, No. 6, 2018.
doi: 10.3390/en11061418.

[25] Rodríguez, D., and Theofilis, V., "On the Birth of Stall Cells on Airfoils," *Theoretical and Computational Fluid Dynamics* Vol. 25, No. 1, 2011, pp. 105-117.
doi:10.1007/s00162-010-0193-7

[26] Rodríguez, D., and Theofilis, V., "Structural Changes of Laminar Separation Bubbles Induced by Global Linear Instability," *Journal of Fluid Mechanics*, Vol. 655, 2010, pp. 280-305.
doi:10.1017/S0022112010000856

[27] Schewe, G., "Reynolds-number Effects in Flow Around More-or-Less Bluff Bodies," *Journal of Wind Engineering and Industrial Aerodynamics*, Vol. 89, No. 14-15, 2001, pp. 1267-1289.
doi: 10.1016/S0167-6105(01)00158-1

[28] Garland, M. G., Santer, M. S., and Morrison, J. F., "Control of Cellular Separation Using Adaptive Surfaces," *Journal of Fluids and Structures*, Vol. 91, Nov. 2019, pp. 102609.
doi: 10.1016/j.jfluidstructs.2019.03.002

[29] Ragni, D., and Ferreira, C., “Effect of 3D Stall-cells on the Pressure Distribution of a Laminar NACA64-418 Wing,” *Experiments in Fluids*, Vol. 57, No. 8, 2016, pp. 127.
doi: 10.1007/s00348-016-2215-8

[30] Gregory, N., Quincey, V. G., O’Reilly, C. L., and Hall, D. J., *Progress Report on Observations of Three-dimensional Flow Patterns Obtained During Stall Development on Aerofoils, and on the Problem of Measuring Two-dimensional Characteristics*, HM Stationery Office: Aeronautical Research Council. C.P. No. 1146, 1971.

[31] Gibeau, B., Gingras, D. and Ghaemi, S., "Evaluation of a Full-Scale Helium-Filled Soap Bubble Generator." *Experiments in Fluids*, Vol. 61, No. 2, 2020, pp. 1-18.
doi: 10.1007/s00348-019-2853-8

[32] Abbott, I. H., and Von Doenhoff, A. E., “Theory of Wing Sections: Including a Summary of Airfoil Data,”. Courier Corporation. 1959.

[33] Velte, C. M., and Hansen, M. O., “Investigation of Flow Behind Vortex Generators by Stereo Particle Image Velocimetry on a Thick Airfoil Near Stall,” *Wind Energy*, Vol. 16, No. 5, 2013, pp. 775-785.
doi: 10.1002/we.1541

[34] Lin, J. C., “Review of Research on Low-profile Vortex Generators to Control Boundary-layer Separation,” *Progress in Aerospace Sciences*, Vol. 38, No. 4-5, 2002, pp. 389-420.
doi: 10.1016/S0376-0421(02)00010-6

[35] Wang, S., and Ghaemi, S., “Effect of Vane Sweep Angle on Vortex Generator Wake,” *Experiments in Fluids*, Vol. 60, No. 1, 2019, pp. 24.
doi: 10.1007/s00348-018-2666-1

[36] Godard, G., and Stanislas, M., “Control of a Decelerating Boundary Layer. Part 1: Optimization of Passive Vortex Generators,” *Aerospace Science and Technology*, Vol. 10, No. 3, 2006, pp. 181-191.
doi: 10.1016/j.ast.2005.11.007

[37] Betterton, J. G., Hackett, K. C., Ashill, P. R., Wilson, M. J., Woodcock, I. J., Tilman, C. P., and Langan, K. J., “Laser Doppler Anemometry Investigation on Sub Boundary Layer Vortex Generators for Flow Control,” *10th symposium on application of laser techniques to fluid mechanics*, Lisbon, 2000, pp. 10-12.

[38] Lin, J., “Control of Turbulent Boundary-Layer Separation Using Micro-Vortex Generators,” *30th Fluid Dynamics Conference*, 1999, pp. 3404.

doi: 10.2514/6.1999-3404

[39] Ashill, P., J. Fulker, and K. Hackett., “Studies of Flows Induced by Sub Boundary Layer Vortex Generators (SBVGs).” *40th AIAA aerospace sciences meeting & exhibit,* 2002, pp. 968.

doi: 10.2514/6.2002-968

[40] Westerweel, Jerry, and Fulvio Scarano. "Universal outlier detection for PIV data." *Experiments in fluids,* Vol. 39, No. 6, 2005, pp. 10.

doi: 10.1007/s00348-005-0016-696-1100.

[41] Raffel, M., Willert, C. E., Scarano, F., Kähler, C. J., Wereley, S. T., and Kompenhans, J., “Particle Image Velocimetry: A Practical Guide,” 2018, Springer.

doi: 10.1007/978-3-319-68852-7

[42] Wieneke, B., “Volume Self-calibration for 3D Particle Image Velocimetry,” *Experiments in fluids,* Vol. 45, No. 4, 2008, pp. 549-556.

doi: doi.org/10.1007/s00348-008-0521-5

[43] Gibeau, B., and Ghaemi, S., “A Modular, 3D-printed Helium-filled Soap Bubble Generator for Large-scale Volumetric Flow Measurements,” Experiments in Fluids, Vol. 59, No.12, 2018, pp. 178.

doi:10.1007/s00348-018-2634-9

[44] Schanz, D., Gesemann, S., Schröder, A., Wieneke, B., and Novara, M., “Non-uniform Optical Transfer Functions in Particle Imaging: Calibration and Application to Tomographic Reconstruction,” *Measurement Science and Technology,* Vol. 24, No. 2, 2012, pp. 024009.

doi: 10.1088/0957-0233/24/2/024009

[45] Schanz, D., Gesemann, S., and Schröder, A., “Shake-The-Box: Lagrangian Particle Tracking at High Particle Image Densities,” *Experiments in fluids,* Vol. 57, No. 5, 2016, pp. 70.

doi: 10.1007/s00348-016-2157-1

[46] Ebrahimian, M., Sanders, R. S., and Ghaemi, S., “Dynamics and Wall Collision of Inertial Particles in a Solid–Liquid Turbulent Channel Flow,” *Journal of Fluid Mechanics,* Vol. 881, 2019, pp. 872-905.

doi:10.1017/jfm.2019.749

[47] Rowin, W. A., and Ghaemi, S., “Streamwise and Spanwise Slip over a Superhydrophobic Surface,” *Journal of Fluid Mechanics,* Vol. 870, 2019, pp. 1127-1157.

doi:10.1017/jfm.2019.225